iMed

SCIEPublish

Communication

Nanosecond Laser-Driven Proton FLASH Spares Normal Tissue Cells by Sustaining Mitochondrial Homeostasis and Attenuating Ferroptosis

Changsheng Shao [1,†], Yu Zhang [2,†], Pengzhi He [3,†], Xin Yu [1,4], Wenjie Peng [2,5], Junfeng Chen [2,5], Haotian Hu [2,5], Yiying Wang [3], Mei Xiao [6], Chao Liu [7], Li Sui [8], Tianyuan Dai [9], Xiangkui Mu [10], Xianghong Jia [3,11,*], Jian-Hui Bin [2,5,*] and Qing Huang [1,4,*,‡]

[1] Institute of Health and Medical Technology, Hefei Institutes of Physical Science, Chinese Academy of Sciences, Hefei 230031, China; shaochangsheng@hmfl.ac.cn (C.S.); yu_xin@mail.ustc.edu.cn (X.Y.)
[2] State Key Laboratory of Ultra-Intense Laser Science and Technology, Shanghai Institute of Optics and Fine Mechanics, Chinese Academy of Sciences, Shanghai 201800, China; zhang_yu@siom.ac.cn (Y.Z.); pengwenjie@siom.ac.cn (W.P.); chenjf@siom.ac.cn (J.C.); huhaotian23@mails.ucas.ac.cn (H.H.)
[3] Shandong Key Laboratory of Space Environment and Exploration Technology, School of Space Science and Technology, Shandong University, Weihai 264209, China; hpz@mail.sdu.edu.cn (P.H.); 202417817@mail.sdu.edu.cn (Y.W.)
[4] Science Island Branch of Graduate School, University of Science and Technology of China, Hefei 230052, China
[5] Center of Materials Science and Optoelectronics Engineering, University of Chinese Academy of Sciences, Beijing 101408, China
[6] Shanghai Proton and Heavy Ion Center, Shanghai 4365, China; mei.xiao@sphic.org.cn (M.X.)
[7] School of Biomedical Engineering, Anhui Medical University, Hefei 230032, China; liuchao9706@ahmu.edu.cn (C.L.)
[8] Department of Nuclear Physics, China Institute of Atomic Energy, Beijing 102413, China; lisui@ciae.ac.cn (L.S.)
[9] Department of Radiation Oncology Physics and Technology, Shandong Cancer Hospital and Institute, Shandong First Medical University and Shandong Academy of Medical Sciences, Jinan 250117, China; daity@sd-cancer.com (T.D.)
[10] Shandong Proton, Heavy Ion and Neutron Therapy Center, Shandong First Medical University Affiliated Tumor Hospital, Jinan 250117, China; muxk@sd-cancer.com (X.M.)
[11] College of Science, Xizang University, Lhasa 850000, China

* Corresponding authors. E-mails: jiaxh@sdu.edu.cn (X.J.); jianhui.bin@siom.ac.cn (J.-H.B.); huangq@ipp.ac.cn (Q.H.)

† These authors contributed equally to this work.
‡ This author is the primary corresponding author.

Received: 12 April 2026; Revised: 18 May 2026; Accepted: 22 June 2026; Available online: 13 July 2026

ABSTRACT: Radiotherapy's clinical utility remains fundamentally constrained by the collateral damage to healthy tissues. Ultra-high dose rate (UHDR) irradiation, or FLASH-radiotherapy (FLASH-RT) has emerged as a transformative paradigm to mitigate such toxicity. However, the biological effects of FLASH-RT on the high-efficiency of tumor killing and normal tissue sparing remain poorly understood. In this work, we utilized a petawatt-class laser-plasma acceleration (LPA) platform to deliver discrete 12.9-nanosecond proton pulses at an extreme instantaneous dose rate of 1.94×10^7 Gy/s. This temporal singularity achieved a profound sparing effect in normal bronchial epithelial cells, evidenced by a nine-fold reduction in the lethal α coefficient (from 0.47 to 0.05 Gy^{-1}), while maintaining full tumoricidal potency against lung adenocarcinoma. Mechanistically, we demonstrated that LPA-FLASH could effectively

bypass the ATF3-mediated stress response and circumvent the subsequent ferroptotic cascade. This molecular evasion could preserve the mitochondrial cristae integrity and trigger an adaptive bioenergetic ATP surge—a hallmark of metabolic resilience exclusively in healthy tissue cells. Therefore, our findings identify ferroptosis-mediated mitochondrial integrity as a unifying framework for selective normal-tissue protection at the physical limits of radiation delivery, and establish LPA-FLASH-RT as a potent, compact modality for next-generation oncology.

Keywords: FLASH-radiotherapy (FLASH-RT); Laser-plasma acceleration (LPA); Mitochondrial integrity; Ferroptosis; Normal tissue cells sparing

1. Introduction

Radiotherapy is a cornerstone of comprehensive cancer treatment; however, its clinical efficacy is limited by a narrow therapeutic window resulting from collateral damage to healthy stromal tissues [1]. FLASH radiotherapy (FLASH-RT) is a technique that administers ultra-high dose rate (UHDR) irradiation in less time without compromising tumor treatment [2–4]. Preclinical studies across diverse animal models have consistently demonstrated that FLASH-RT significantly mitigates acute and late complications in normal tissues while maintaining tumor control comparable to conventional radiotherapy (CONV-RT), a paradigm-shifting biological selectivity termed the "FLASH effect" [5–7].

Despite the promising therapeutic potential of FLASH-RT, the underlying radiobiological mechanisms remain a subject of intense debate. Current hypotheses encompass rapid oxygen depletion leading to transient radiochemical hypoxia [8], alteration of radical-radical recombination [9], and the preservation of mitochondrial function [10]. Recent evidence also suggests that ferroptosis—an iron-dependent form of regulated cell death characterized by lipid peroxidation [11]—may be a pivotal executioner of the FLASH-mediated sparing effect [12,13].

A defining characteristic of FLASH-RT is its extreme instantaneous dose rate. To date, most FLASH research has utilized traditional radiofrequency linear accelerators or cyclotrons operating in the microsecond regime. Importantly, recent advances in compact laser-plasma acceleration (LPA) have opened a fundamentally different physical regime. Laser-driven proton sources utilize petawatt-class femtosecond laser pulses to generate proton beams with durations in the picosecond-to-nanosecond range, achieving instantaneous dose rates exceeding 10^9 Gy/s—six orders of magnitude higher than conventional FLASH systems [13–15].

In this study, by employing a high-repetition-rate laser-driven proton platform at the Shanghai Institute of Optics and Fine Mechanics (SIOM) (so-called SIOM HLDP platform). We sought to reveal the LPA-FLASH effect in the petawatt–picosecond regime and to explore its molecular underpinnings. By delivering protons as discrete 12.9 ns pulses with an extreme instantaneous dose rate, we systematically compared the biological impact on human A549 lung adenocarcinoma cells and BEAS-2B normal bronchial epithelial cells with that of conventional clinical protons (CONV-RT). Through an integrated approach—incorporating 3D light-sheet fluorescence microscopy for subcellular morphometric quantification, transmission electron microscopy (TEM) for ultrastructural analysis, and functional mitochondrial assays—we demonstrated that LPA-FLASH-RT could give rise to a differential biological response characterized by the selective preservation of mitochondrial cristae in normal cells. By characterizing the spatio-temporal dynamics of the special ATF3-mediated ferroptotic axis, we revealed that the temporal singularity of laser-driven protons could probe a transcriptional blind spot, effectively bypassing lethal oxidative stress cascades. Therefore, this study may help to establish LPA-FLASH-RT as a promising modality that

highlights the interplay between DNA damage and metabolic resilience, and may provide mechanistically informed groundwork for next-generation radiotherapy.

2. Materials and Methods

2.1. Cell Lines and Culture Conditions

Human lung adenocarcinoma cells (A549) and human normal bronchial epithelial cells (BEAS-2B) were obtained from the American Type Culture Collection (ATCC, Manassas, VA, USA). Cells were maintained in DMEM (Gibco, Thermo Fisher Scientific, Waltham, MA, USA) supplemented with 10% fetal bovine serum (FBS) and 1% penicillin-streptomycin in a humidified incubator at 37 °C with 5% CO_2. For all irradiation experiments, cells were seeded onto custom-designed culture dishes sealed with a 2 μm Mylar foil base. This thin interface was critical for minimizing proton energy loss and ensuring accurate dose delivery to the cell monolayer.

2.2. Proton Irradiation and Dosimetry

Laser-driven FLASH-RT: Ultra-high dose rate irradiation was performed using a 200 TW Laser System [16,17]. Protons were accelerated to 7 MeV and delivered in pulses (repetition rate: 0.1 Hz; pulse width: 12.9 ns). The system achieved an extreme instantaneous dose rate of 1.94×10^7 Gy/s. Cells were irradiated within a vacuum-compatible chamber, with the beam passing through a vacuum window before reaching the Mylar foil interface.

Conventional-RT (CONV-RT): Standard dose-rate irradiation was conducted using a SIEMENS IONTRIS Accelerator System (Siemens Healthineers, Erlangen, Germany). A proton beam with an initial energy of 221 MeV was degraded using a solid water phantom so that the protons reached the Bragg peak region at the position of the cell monolayer, corresponding to proton energies in the few-MeV range after passing through the beamline materials. The dose rate was maintained at a steady-state 0.08 Gy/s.

Dosimetry: All proton doses (2, 5, and 10 Gy) were calibrated and verified using Gafchromic HD-V2 radiochromic film (Ashland Inc., Wilmington, DE, USA). The principle relies on the dose-dependent color change of the film, which was pre-calibrated against a clinical proton accelerator using an Epson Perfection V600 scanner (Seiko Epson Corporation, Suwa, Nagano, Japan). RCF was placed immediately behind the cell holder, parallel to the rear Mylar window. The proton path through all absorbers (including the Kapton vacuum window, air gap, Mylar films, cell layer, and additional light-tight foils) was modelled using SRIM Monte-Carlo simulations. This yielded the ratio of dose deposition in the cell monolayer to that in the RCF. The measured RCF dose (converted to optical density from scanned images) was then corrected by this ratio to obtain the actual dose delivered to the cells.

2.3. Clonogenic Survival Assay and LQ Modeling

Following irradiation, cells were immediately trypsinized and re-seeded into 6-well plates at densities optimized for each dose. After 10–14 days of incubation, colonies were fixed with methanol and stained with 0.5% crystal violet. Colonies consisting of >50 cells were counted manually. The survival fraction (SF) was calculated and fitted using the linear-quadratic (LQ) model: $S = e^{-(\alpha D+\beta D^{\wedge}2)}$, where D is the dose and α, β are the radiosensitivity coefficients.

2.4. Immunofluorescence Staining

Cells were fixed with 4% paraformaldehyde (PFA) for 15 min and permeabilized with 0.5% Triton X-100. After blocking with 5% BSA, samples were incubated overnight at 4 °C with primary antibodies against γ-H2AX (1:500, Proteintech, Wuhan, China) or ATF3 (1:200, Proteintech, Wuhan, China). Cells were then labeled with fluorophore-conjugated secondary antibodies and counterstained with DAPI.

Images were acquired using a Leica SP8 confocal microscope (Leica Microsystems, Wetzlar, Germany). For γ-H2AX, DNA double-strand breaks (DSBs) were quantified as the number of foci per nucleus. For ATF3, the mean fluorescence intensity (MFI) within the nucleus was calculated using ImageJ (version 2.16.0, National Institutes of Health, Bethesda, MD, USA).

2.5. Assessment of Oxidative Stress and Ferroptosis Markers

ROS and Lipid Peroxidation: Intracellular reactive oxygen species (ROS) were measured 1 h post-irradiation using the H_2DCFDA probe (10 μM, Thermo Fisher Scientific, Waltham, MA, USA). ROS levels were quantified via flow cytometry (BD LSRFortessa, BD Biosciences, San Jose, CA, USA). Lipid peroxidation (LPO) was assessed 4 h post-irradiation using the Liperfluo probe (1 μM, Dojindo Molecular Technologies, Kumamoto, Japan). LPO-specific fluorescence was captured via confocal microscopy and analyzed as relative fluorescence units (RFU).

Labile Iron Pool (Fe^{2+}): Intracellular ferrous iron levels were evaluated 4 h post-irradiation using the FerroFarRedfluorescent probe (1 μM, Goryo Chemical, Sapporo, Japan). After 30 min of incubation at 37 °C, cells were imaged using confocal microscopy (Ex/Em: 635/660 nm). Intensity was quantified as MFI to assess the correlation between iron overload and lipid damage.

2.6. Mitochondrial Functional and Structural Analysis

ATP and MMP: Intracellular ATP was quantified 4 h post-irradiation using a luminescence-based assay kit (Beyotime Biotechnology, Shanghai, China) and normalized to total protein concentration. Mitochondrial membrane potential (MMP) was determined using the JC-1probe (Thermo Fisher Scientific, Waltham, MA, USA). The ratio of red (aggregates) to green (monomers) fluorescence was calculated to evaluate mitochondrial polarization.

Transmission Electron Microscopy (TEM): Cells were fixed in 2.5% glutaraldehyde and post-fixed in 1% osmium tetroxide. Samples were dehydrated and embedded in epoxy resin. Ultrathin sections (70–90 nm) were stained with uranyl acetate and lead citrate and imaged using a Hitachi H-7650 TEM (Hitachi High-Technologies, Tokyo, Japan) at 80 kV. Mitochondria were classified as ferroptotic based on characteristic shrinkage, loss of cristae, and increased membrane density.

2.7. 3D Mitochondrial Network Dynamics

For whole-cell morphological analysis, cells were stained with MitoTracker Deep Red FM. Z-stack images were acquired using a light-sheet fluorescence microscope (Wuhan Smart-View Biotechnology, Wuhan, China) with a Z-step of 100 nm. 3D reconstruction and surface rendering were performed using Imaris 10.1. For 3D morphometric analysis, we quantified mitochondrial sphericity and individual organelle volume, two established markers of fragmentation versus tubular network organization. Sphericity increases as mitochondria transition from elongated, reticular structures to small, globular fragments, whereas volume decreases with loss of fused networks and mitochondrial biomass. Network skeletonization was performed using the MiNA plugin in ImageJ to calculate branching and complexity.

2.8. Statistical Analysis

All experiments were performed in at least three independent biological replicates. Data are presented as mean ± s.d. Statistical significance was evaluated using one-way ANOVA followed by Tukey's post-hoc test for multiple comparisons or Student's *t*-test for pairwise comparisons. $p < 0.05$ was considered statistically significant (*, $p < 0.05$; **, $p < 0.01$; ***, $p < 0.001$). All analyses were conducted using GraphPad Prism 10.2.

3. Results

3.1. GEANT4 Monte Carlo Simulation of Proton Energy Deposition Spectra in the Cell Layer under LPA-FLASH-RT and CONV-RT

To determine whether biological differences between LPA-FLASH-RT and CONV-RT at equivalent physical doses (2–10 Gy) arise from distinct cellular energy deposition patterns, we performed Geant4 Monte Carlo simulations to characterize proton energy deposition spectra in a 5 μm cellular layer under both irradiation modalities.

For the LPA-FLASH-RT configuration, we modeled 7.8 MeV protons traversing a series of upstream materials representative of a laboratory-scale LPA system: a 22 μm aluminum foil, 100 μm Kapton window, 45 mm of air, and 3.6 μm Mylar foil, before interacting with the cellular layer (Figure 1a). This geometry produced a sharp, nearly monoenergetic incident proton energy spectrum with a prominent peak at approximately 6.5 MeV (Figure 1b). Strikingly, when these protons deposited energy within the 5 μm aqueous cellular layer, the resulting energy deposition spectrum displayed a narrow, concentrated peak at approximately 55 keV (Figure 1c), demonstrating that the LPA beam maintains exceptionally uniform dose deposition across the cellular volume.

In contrast, the CONV-RT configuration simulated a clinically realistic scenario in which 221 MeV protons were transmitted through a composite beamline consisting of 80 cm of air, 30 cm of solid water phantom (98% C_8H_8 + 2% TiO_2, ρ = 1.045 g/cm^3), 10 cm of air, and 0.3 mm polyvinyl chloride, before reaching the cellular layer. The solid water thickness was chosen so that the Bragg peak would occur near the cellular layer after accounting for upstream energy losses. Under these clinically representative conditions, the incident proton energy spectrum became substantially broadened, exhibiting a relatively heterogeneous distribution spanning 8–14 MeV (Figure 1d). This energy broadening, inherent to clinical beamline design, directly translated into a broader energy deposition spectrum within the cellular layer, with a primary peak at approximately 13 keV and an extended low-energy tail (Figure 1e).

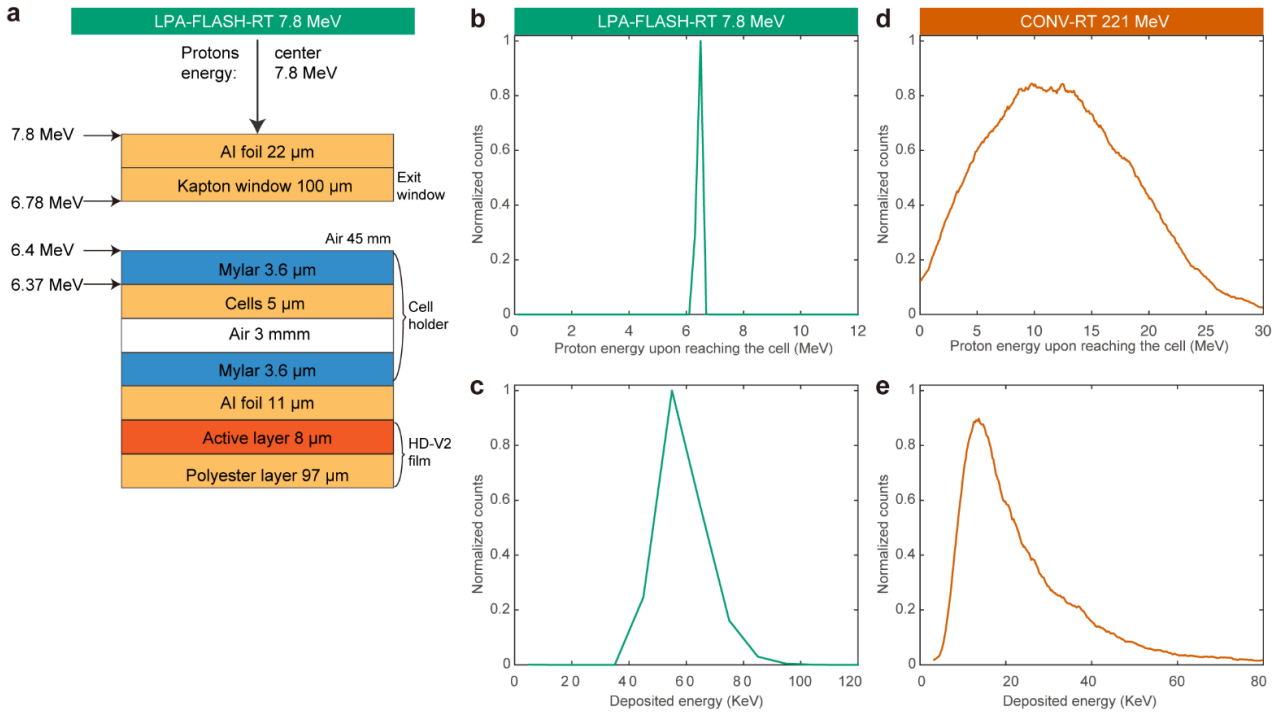

Figure 1. Geant4-simulated energy deposition spectra of protons under representative irradiation conditions. (**a**) Schematic diagram and dosimetric calibration of the proton dose delivery system for laser-plasma acceleration (LPA)-based FLASH-radiotherapy configurations. (**b**) Incident proton energy spectrum incident on the cellular layer in the LPA-FLASH-RT system, characterized by a sharp, monoenergetic peak at approximately 6.5 MeV (nominal beam energy: 7.8 MeV). (**c**) Corresponding

energy deposition (dose) spectrum deposited within the 5 μm aqueous cellular layer for the incident spectrum shown in (**b**), exhibiting a narrow, concentrated peak at approximately 55 keV, typical of low-divergence FLASH-RT beams. (**d**) Incident proton energy spectrum for the CONV-RT system following passage through the composite clinical beamline (initial energy: 221 MeV), displaying a relatively broad, heterogeneous energy distribution with a main peak spanning 8–14 MeV due to upstream scattering and modulation components. (**e**) Corresponding energy deposition spectrum in the 5 μm aqueous cellular layer for the incident spectrum in (**d**), showing a broader distribution with a primary peak at approximately 13 keV and an extended low-energy tail characteristic of conventional modulated proton therapy. Green curves represent LPA-FLASH-RT configuration; red/orange curves represent CONV-RT configuration. All Monte Carlo simulations employed 1×10^7 primary protons per configuration to ensure adequate statistical reliability and spectral resolution.

Both simulations employed 1×10^7 primary protons. LPA-FLASH-RT delivered ~4-fold higher peak dose with uniform distribution, while CONV-RT exhibited the energy heterogeneity typical of clinical modulated beams. These distinct physical parameters define the dosimetric basis for comparing radiobiological effectiveness between the two modalities.

3.2. LPA-FLASH-RT Establishes a Superior Therapeutic Window by Selectively Sparing Normal Cells

To investigate whether the extreme temporal compression of laser-driven protons translates into a biological advantage, we utilized the 200 TW laser-driven proton source at the SIOM HLDP platform. This system generates protons in discrete, ultra-short pulses (Δt = 12.9 ns), delivering 0.25 Gy per shot and achieving an extreme instantaneous dose rate (IDR) of 1.94×10^7 Gy/s (hereafter referred to as LPA-FLASH-RT). We directly compared this regime with a conventional proton accelerator operating at a standard clinical dose rate of 0.08 Gy/s (hereinafter CONV-RT) (Figure 2a,b).

Clonogenic survival assays revealed that this nine-order-of-magnitude increase in dose rate did not compromise tumoricidal efficacy. survival curves and lethal α values for A549 tumor cells were indistinguishable between LPA-FLASH-RT (α = 0.46 Gy^{-1}) and CONV-RT (α = 0.55 Gy^{-1}, $p > 0.05$). Conversely, normal BEAS-2B cells exhibited a profound survival advantage under LPA-FLASH-RT, with the α value plummeting nine-fold (from 0.47 to 0.052 Gy^{-1}, $p < 0.001$, Figure 2c), confirming potent normal-tissue sparing without sacrificing malignant-cell kill.

The profound nine-fold reduction in the lethal α value of normal cells suggested that the nanosecond pulse may alter the balance between early radiation injury and cellular recovery. To examine this early response, we quantified γ-H2AX foci 0.5 h post-irradiation. Both modalities induced substantial DNA double-strand breaks in A549 cells at 10 Gy, with no obvious difference between LPA-FLASH-RT and CONV-RT. In BEAS-2B cells, LPA-FLASH-RT showed a modest reduction in γ-H2AX foci relative to CONV-RT at 5 Gy, but the overall effect was limited (Figure 2d–f). Importantly, the magnitude of this DNA damage difference was smaller than the survival difference, suggesting that the marked normal-cell sparing effect cannot be explained by initial DSB formation alone. Rather, LPA-FLASH-RT may influence downstream processes such as redox recovery and metabolic adaptation, which together determine cell fate after irradiation.

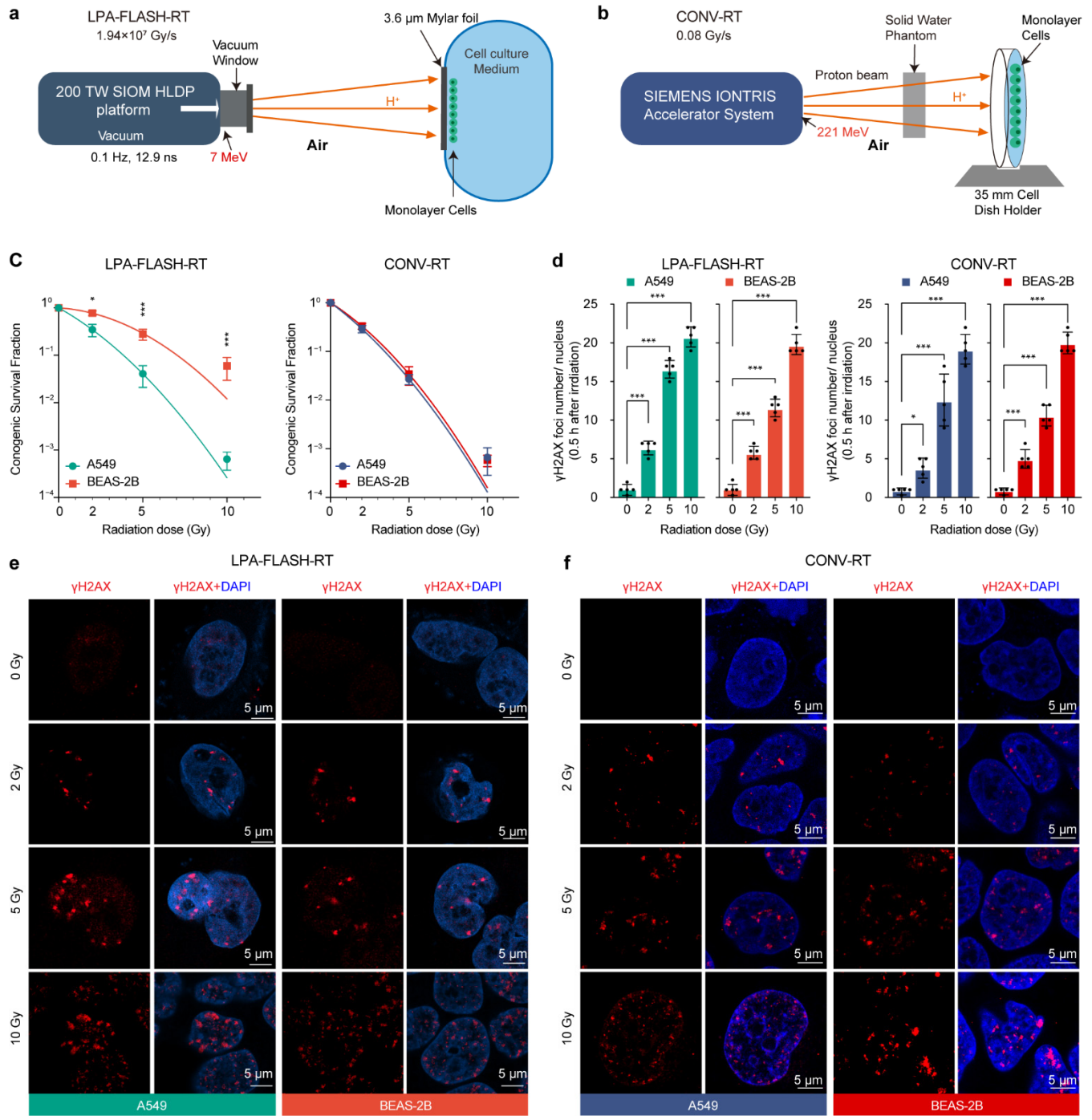

Figure 2. Differential biological effects of laser-driven FLASH versus conventional proton irradiation. (**a**,**b**) Schematic illustrations of the experimental setups for the laser-driven FLASH proton irradiation (LPA-FLASH-RT) system (**a**) and the conventional proton irradiation (CONV-RT) system (**b**). (**c**) Clonogenic survival fractions (SF) of BEAS-2B normal lung epithelial cells and A549 lung adenocarcinoma cells. The left panel shows survival curves under LPA-FLASH-RT, and the right panel shows survival curves under CONV-RT. Data were fitted using the linear-quadratic model ($n = 3$ independent experiments). (**d**) Quantification of DNA double-strand breaks as measured by the number of γ-H2AX foci per cell ($n = 5$, random fields). (**e**,**f**) Representative immunofluorescence images of γ-H2AX foci (red) and DAPI-stained nuclei (blue) in cells at 0.5 h post-irradiation with LPA-FLASH-RT (**e**) and CONV-RT (**f**). Scale bar, 5 μm. *, significant difference ($p < 0.05$); ***, highly significant difference ($p < 0.001$).

3.3. LPA-FLASH-RT Bypass the Pro-Ferroptotic ATF3 Stress-Response Axis in Normal Cells

At 1 h after irradiation, intracellular ROS displayed distinct dose–response patterns between tumour and normal cells under each irradiation modality (Figure 3a). With LPA-FLASH-RT, A549 cells showed a

clear, dose-dependent increase in ROS, whereas BEAS-2B cells remained close to baseline across 2–10 Gy; at 10 Gy, ROS in A549 was almost 1.7-fold higher than in BEAS-2B (908 ± 9.3 *vs*. 527 ± 12 RFU). By contrast, under CONV-RT both A549 and BEAS-2B cells exhibited a pronounced dose-dependent ROS elevation, and at 10 Gy, both cell types reached similarly high ROS levels (1012 ± 103 *vs*. 895 ± 13 RFU), indicating that the normal-cell sparing observed with FLASH is largely lost at conventional dose rate.

Consistent with these early ROS profiles, lipid peroxidation (LPO) and labile iron (Fe^{2+}) accumulation at 4 h also diverged between tumour and normal cells in a modality-dependent manner (Figure 3b–d). For LPA-FLASH-RT, A549 cells developed marked, dose-dependent increases in LPO and Fe^{2+}, whereas BEAS-2B cells showed minimal changes even at 10 Gy (LPO 163 ± 15 RFU; Fe^{2+} 5.6 ± 1.1 MFI). By contrast, CONV-RT induced strong, dose-dependent increases in both readouts in A549 and BEAS-2B cells, driving normal cells into a high-damage state at 10 Gy (LPO 714 ± 74 RFU; Fe^{2+} 11.6 ± 1.8 MFI, $p < 0.001$ *vs*. LPA-FLASH-RT). A strong positive correlation between LPO and Fe^{2+} across conditions confirmed that lipid peroxidation tightly tracks iron loading in this system (Figure 3e).

To decipher the molecular gatekeeper of this selective protection, we focused on the stress-responsive transcription factor ATF3 (Figure 3f). We hypothesized that the nanosecond pulse exploits a transcriptional blind spot, bypassing ATF3-mediated suppression of the SLC7A11 antioxidant system. While both radiation types strongly induced nuclear ATF3 in A549 cells (~124–126 MFI at 10 Gy) (Figure 3g,h), LPA-FLASH-RT kept ATF3 at near-baseline levels in BEAS-2B cells (13.8 ± 1.5 MFI). This protection was absent under CONV-RT, which significantly upregulated ATF3 in normal cells (98.5 ± 15.1 MFI, $p < 0.001$). These data demonstrate that the temporal singularity of LPA-FLASH-RT keeps normal cells below the kinetic threshold for ATF3 activation, thereby bypassing the pro-ferroptotic axis.

3.4. Selective Preservation of Mitochondrial Cristae and Bioenergetic Efficiency under LPA-FLASH Irradiation

Building on the evasion of the ATF3-ferroptotic axis, we assessed downstream bioenergetic consequences at 4 h post-irradiation. In A549 tumor cells, both modalities induced severe metabolic collapse at 5 Gy, characterized by depleted ATP and dissipated mitochondrial membrane potential (MMP) (Figure 4a,b). In normal BEAS-2B cells, however, LPA-FLASH-RT uniquely triggered a compensatory ATP surge (9.4 ± 0.2 RFU) and fully maintained MMP (1.03 ± 0.3 of control, $p > 0.05$), contrasting sharply with the profound failure induced by CONV-RT. Ultrastructural (TEM) analysis mirrored this functional dichotomy (Figure 4c). While both modalities drove >70% of tumor mitochondria into a “ferroptotic morphology” (characterized by cristae loss and membrane condensation), LPA-FLASH-RT almost completely shielded normal cells from this structural degradation (10.2 ± 3.4% damaged mitochondria *vs*. 68.4 ± 9.1% under CONV-RT, $p < 0.001$; Figure 4d).

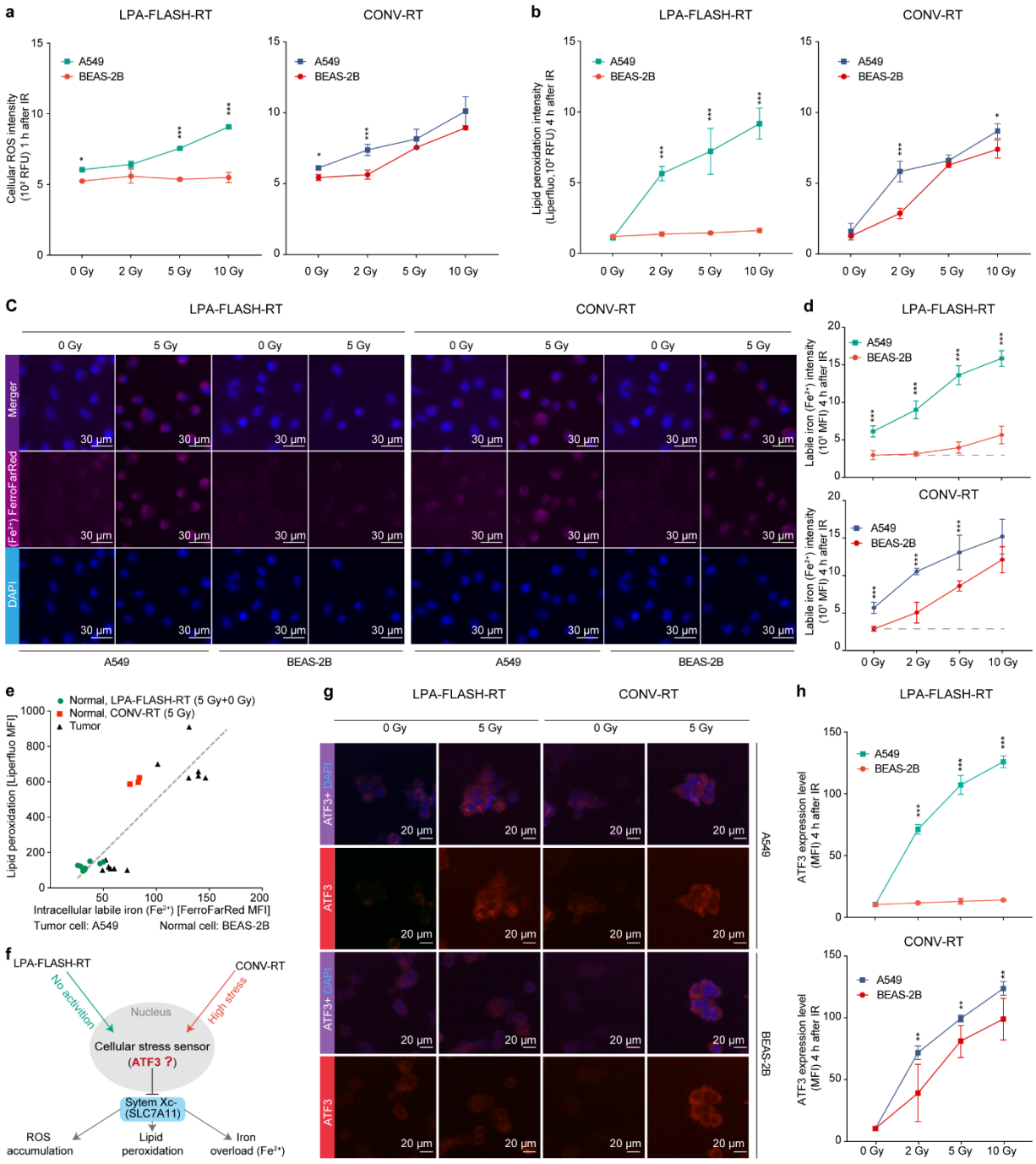

Figure 3. FLASH irradiation mitigates ferroptosis-related oxidative stress and iron overload by bypassing ATF3 activation. (**a**,**b**) Quantification of intracellular oxidative stress markers in BEAS-2B and A549 cells. Intracellular ROS levels (**a**) were assessed using the H_2DCFDA probe, and lipid peroxidation (**b**) was measured using the Liperfluo probe. In both (**a**,**b**), the left panels show results for LPA-FLASH-RT and the right panels for CONV-RT. Data are expressed as relative fluorescence units. (**c**) Representative fluorescence microscopy images of the labile iron pool (Fe^{2+}) levels at 4 h post-irradiation. (**d**) The upper panel displays data for FLASH-RT, and the lower panel for CONV-RT. Scale bar, 30 μm. (**e**) Pearson correlation analysis between intracellular Fe^{2+} levels and lipid peroxidation (Liperfluo intensity). (**f**) Schematic hypothesis illustrating ATF3 as a potential cellular stress sensor that triggers the cascade of ROS accumulation, lipid peroxidation, and iron overload. (**g**) Representative immunofluorescence images showing ATF3 expression and localization. (**h**) Dose-dependent quantification of ATF3 expression levels at 4 h post-irradiation (0, 2, 5, and 10 Gy). The upper panel corresponds to LPA-FLASH-RT, and the lower panel to CONV-RT. *, significant difference ($p < 0.05$); **, very significant difference ($p < 0.01$); ***, highly significant difference ($p < 0.001$).

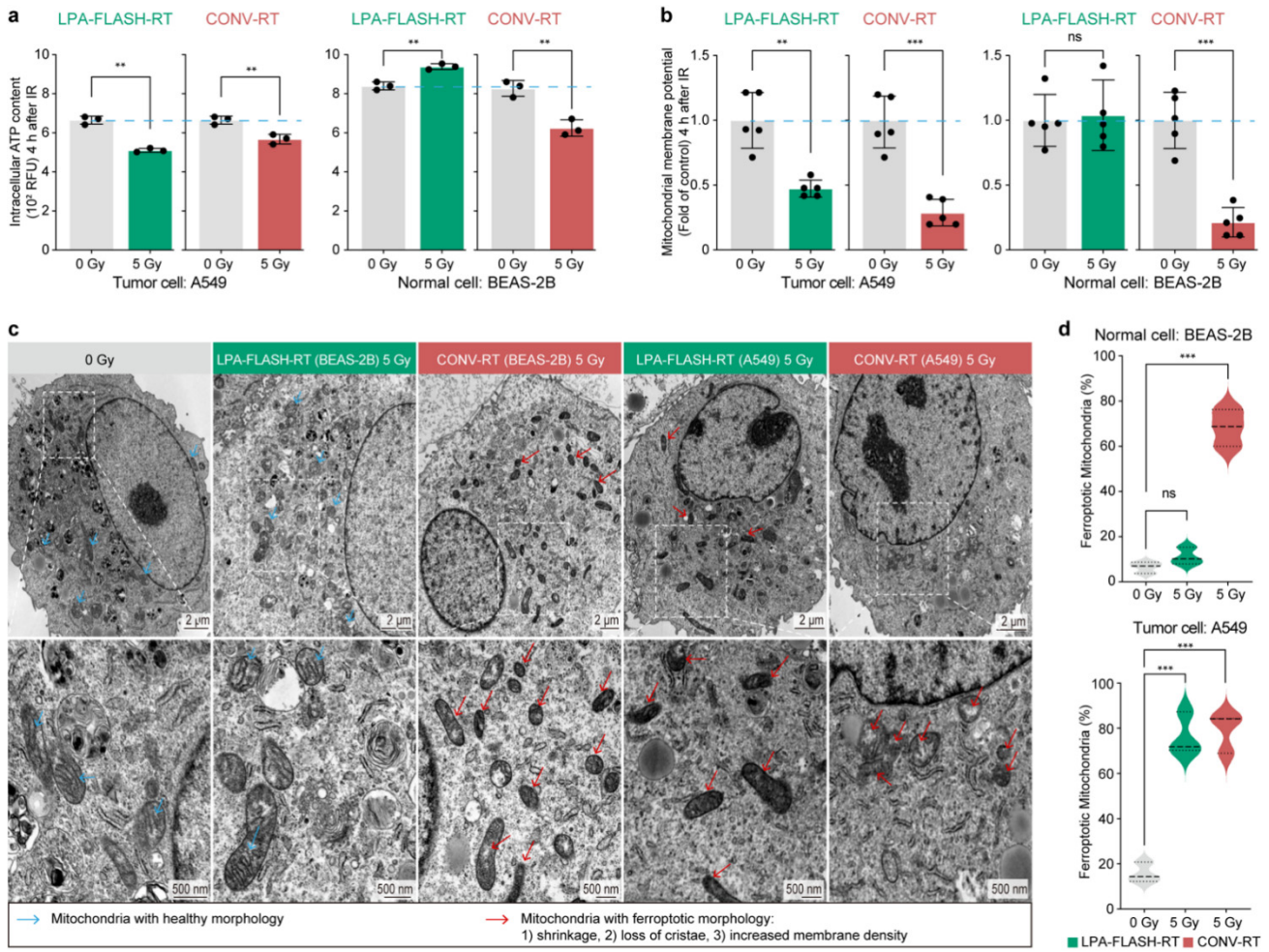

Figure 4. FLASH irradiation preserves mitochondrial bioenergetics and ultrastructural integrity in normal tissues. (**a**,**b**) Assessment of mitochondrial function in BEAS-2B and A549 cells at 4 h post-irradiation. Intracellular ATP levels (**a**) and the mitochondrial membrane potential (**b**), indicated by the ratio of red (aggregates) to green (monomers) JC-1 fluorescence, were normalized to non-irradiated controls. (**c**) Representative transmission electron microscopy (TEM) images showing mitochondrial morphology. The upper panels display low-magnification overviews (Scale bar, 20 μm), and the lower panels show high-magnification insets of the selected regions (Scale bar, 500 nm). Blue arrows indicate healthy mitochondria with intact cristae, while red arrows indicate mitochondria with characteristic ferroptotic features (shrinkage, membrane densification, and cristae loss). (**d**) Quantification of the percentage of mitochondria exhibiting ferroptotic morphology, presented as violin plots. The upper panel shows results for A549 tumor cells, and the lower panel for BEAS-2B normal cells. Green distributions represent LPA-FLASH-RT (5 Gy), and red distributions represent CONV-RT (5 Gy). Data are presented as mean ± s.d. for (**a**,**b**) ($n = 3$ independent experiments) and as distribution density for (**d**) ($n = 3$ random fields). ns, no significant difference ($p > 0.05$); **, very significant difference ($p < 0.01$); ***, highly significant difference ($p < 0.001$).

3.5. Volumetric 3D Imaging Confirms the Structural Resilience of the Global Mitochondrial Reticulum in FLASH-Irradiated Normal Cells

To assess whether the protective effects of LPA-FLASH-RT extend to the global architecture of the mitochondrial network, we performed volumetric 3D light-sheet imaging and quantified mitochondrial sphericity and volume, which report on the degree of network fragmentation versus maintenance of elongated, tubular mitochondria (Figure 5a). Qualitative reconstructions showed that LPA-FLASH-RT preserved a highly interconnected, tubular mitochondrial reticulum in BEAS-2B cells that was indistinguishable from sham controls, whereas CONV-RT converted this network into discrete, punctate fragments (Figure 5b). Quantitatively, under LPA-FLASH-RT BEAS-2B mitochondria remained elongated and voluminous, with sphericity (0.45 ± 0.08) and volume (4.9 ± 1.1 μm^3) values that were indistinguishable

from sham controls ($p > 0.05$). In striking contrast, A549 cells exposed to the same FLASH regimen displayed a highly fragmented mitochondrial network (sphericity 0.75 ± 0.10; volume 1.0 ± 0.4 μm^3), and both parameters differed significantly between A549 and BEAS-2B under LPA-FLASH-RT ($p < 0.001$). Under CONV-RT, BEAS-2B mitochondria shifted towards a more fragmented phenotype, with increased sphericity and reduced volume that approached the values observed in A549 cells, such that the difference between normal and tumour cells was largely attenuated (Figure 5c,d). These comparisons indicate that nanosecond FLASH irradiation preserves a more elongated and interconnected 3D mitochondrial architecture in normal cells, whereas conventional dose-rate irradiation drives both normal and tumour cells towards a similarly fragmented morphology.

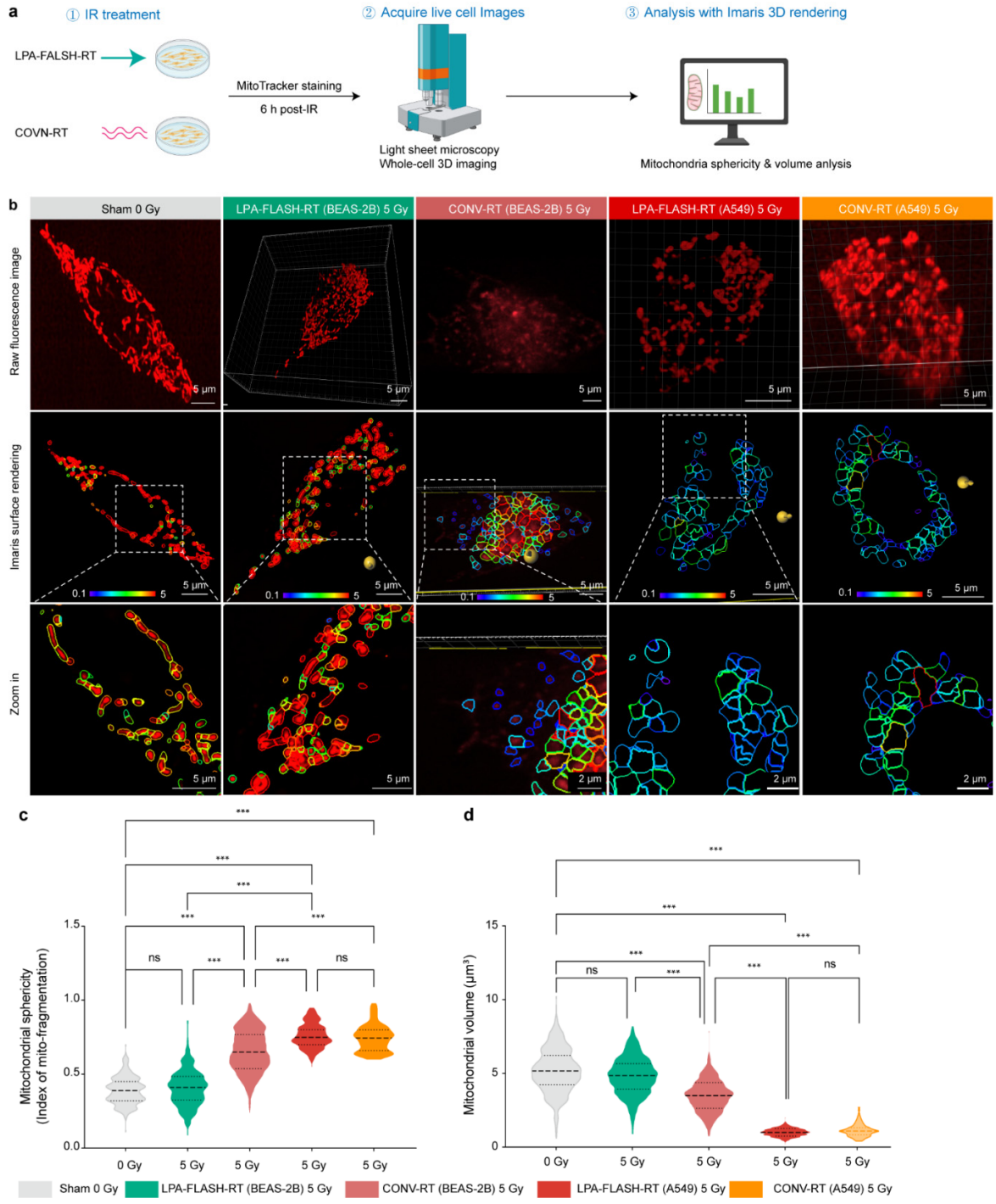

Figure 5. FLASH irradiation preserves mitochondrial network topology and volumetric homeostasis. (**a**) Schematic representation of the experimental and computational pipeline. (**a**) Workflow for cell morphometric quantification by light-sheet

fluorescence microscopy. Normal (BEAS-2B) and malignant (A549) lung cells were subjected to either LPA-FLASH-RT or CONV-RT (5 Gy). Sub-cellular mitochondrial architecture was captured via high-resolution 3D light-sheet fluorescence microscopy (LSFM), followed by 3D surface rendering and morphometric quantification (sphericity and volume) using Imaris software 10.1. (**b**) Representative images of mitochondrial morphology across treatment groups. Top, raw fluorescence signals; middle, corresponding 3D surface-rendered models; bottom, magnified views of the regions indicated by white dashed boxes. Scale bars, 5 μm; zoom-in scale bars, 5 μm and 2 μm. (**c,d**) Quantitative analysis of mitochondrial sphericity (**c**) and mean mitochondrial volume (**d**). Sphericity values approaching 1.0 indicate a fragmented, spherical state. Volume data reflect radiation-induced mitochondrial swelling (BEAS-2B) or degradation (A549) (n = 600). ns, no significant difference ($p > 0.05$); ***, highly significant difference ($p < 0.001$).

4. Discussion

The therapeutic promise of the FLASH effect has been constrained by the limitations of conventional accelerators and a fragmented understanding of its underlying radiobiological mechanisms. In this study, by utilizing the 200-TW beamline at the SIOM HLDP platform, we demonstrated a special "temporal singularity" effect of nanosecond laser-driven proton FLASH, where proton doses were delivered via discrete 12.9 ns pulses at an extreme instantaneous rate of 1.94×10^7 Gy/s. This effect, as elucidated in the 2026 Nature Reviews Cancer analysis by Vozenin et al., suggests a paradigm shift from a narrow focus on radiolytic oxygen depletion (ROD) toward an integrated framework of physicochemical radical kinetics [18]. In this effect, the nanosecond proton delivery induces a "biological decoupling" phenomenon, where the radical-radical recombination is much faster than the activation kinetics of cellular stress-sensing pathways. This mechanism physically reduces the effective yield of oxidative products before they can interact with the biological milieu [19].

While the previous studies of the FLASH effect focused on the attribution of rapid oxygen depletion [8], recent evidence suggests that ferroptosis—an iron-dependent form of regulated cell death—may be a pivotal mediator in the differential response between tumor and normal tissues [9,10]. Specifically, ionizing radiation is known to trigger ferroptosis by elevating ROS and upregulating ACSL4 [20–22]. Therefore, in this study, we hypothesized the execution of FLASH-induced ferroptosis for the primary "biological decoupling" effect, and indeed, we have identified ATF3 as a central regulatory hub in this process. In the FLASH treatment, transcriptional repression of SLC7A11 works as a temporal sensor that critically distinguishes the FLASH-RT response from CONV-RT, thereby sensitizing tumor cells to ultra-high dose rate irradiation. Under CONV-RT, the sustained accumulation of reactive oxygen species (ROS) triggers the transcriptional activation of ATF3, which subsequently represses the SLC7A11/xCT antioxidant system, mobilizing the mitochondrial labile iron pool and catalyzing lethal lipid peroxidation. In contrast, the FLASH pulse appears to deliver the dose within a temporal "blind spot" for ATF3 activation in normal cells, effectively maintaining the cell's antioxidant infrastructure and preventing the transition to ferroptotic cell death (Figure 6).

A vital question addressed by this work is why this protection "FLASH effect" does not extend to malignant A549 cells. We posited that this selectivity is rooted in the pre-existing metabolic divergence between healthy and cancerous tissues [23]. Tumor cells exist in a state of primed oxidative stress and iron metabolic dysregulation, which significantly lowers their threshold for ferroptotic execution. Consequently, the unique temporal structure of a FLASH pulse—while sparing for homeostatic tissue—remains insufficient to prevent the catastrophic failure of their already-strained antioxidant defenses in malignant cells. In contrast, normal BEAS-2B cells leverage the transcriptional blind spot to mount a robust adaptive resilience. Mechanistically, by bypassing the ATF3-SLC7A11 transcriptional blockade, normal cells prevent the ferroptotic chain reaction that typically leads to mitochondrial collapse. Indeed, in this work, we directly observed the remarkable preservation of mitochondria cristae integrity—quantified via TEM and 3D light-sheet imaging, confirming that laser-driven FLASH protons protect the very bioenergetic cores of the cell. In this protected state, the mitochondrial reticulum remains highly interconnected and elongated, providing the structural scaffold necessary for efficient cellular respiration. Particularly, we also

observed the associated ATP surge during the temperal process, and we interpret this ATP surge not merely as a lack of damage, but as an active compensatory response. This functional resilience is mirrored by the dramatic nine-fold reduction in the α value, suggesting that laser-driven FLASH protons enable healthy tissue to maintain, or even temporarily enhance, its metabolic output under radiation stress. To be noted, although the current evidence is limited to two respiratory epithelial cell lines, namely, A549 and BEAS-2B, the fate difference between the cancer and normal cells clearly indicates the mechanism of mitochondrial homeostasis and ferroptosis attenuation. Certainly, for making a universal conclusion, additional validation in other radiation-sensitive normal cell types, using ROS and ferroptosis markers, will be required to determine how broadly this protective effect applies.

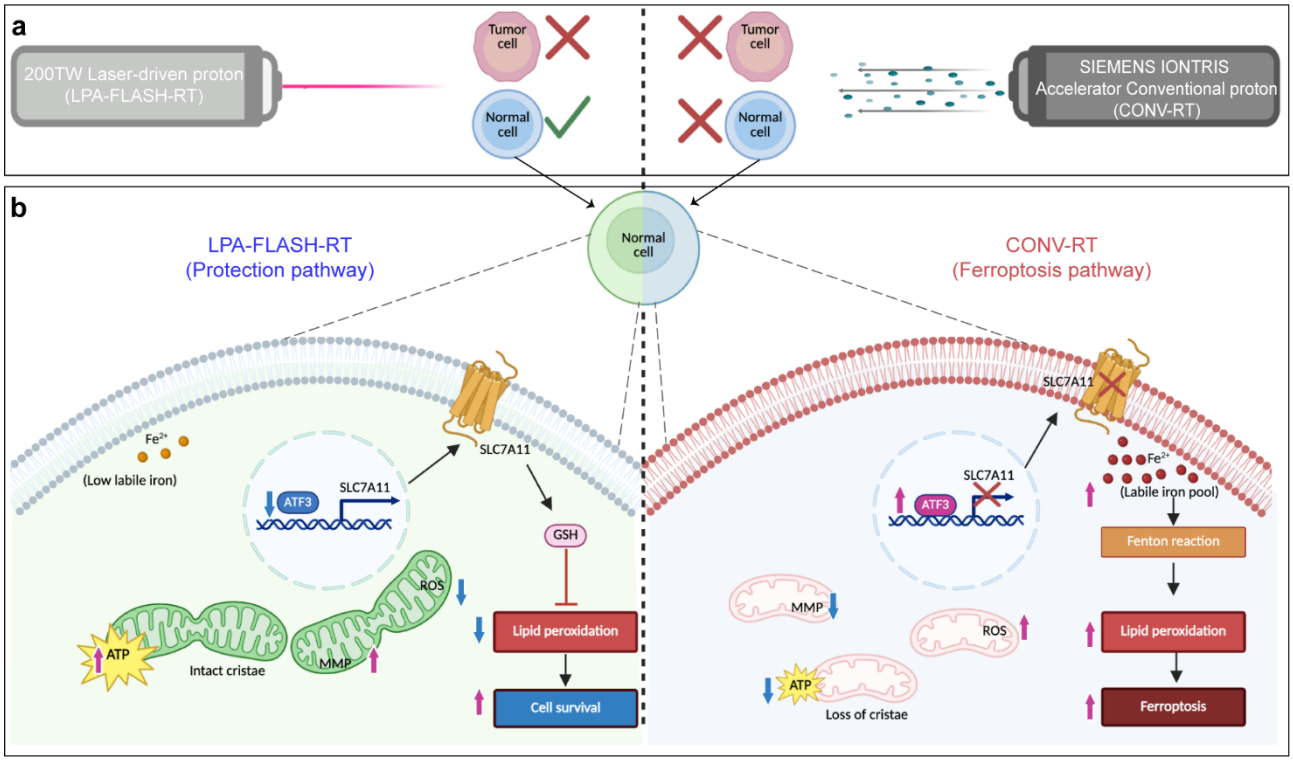

Figure 6. Schematic mechanism of laser-driven ultra-high dose rate proton radiotherapy selectively sparing normal lung cells via the ATF3-ferroptosis axis. (**a**) Macro-level irradiation patterns and cellular survival. FLASH proton beams driven by a petawatt-class laser, characterized by ultra-short pulses and extreme instantaneous dose rates (>107 Gy/s), are shown on the left, while conventional proton (CONV-RT) irradiation with continuous low-intensity beams is illustrated on the right at equivalent doses, LPA-FLASH-RT effectively kills A549 tumor cells while significantly enhancing the clonogenic survival of BEAS-2B normal epithelial cells, demonstrating a pronounced FLASH effect. (**b**) The molecular interplay governing the differential fate of normal cells. Left panel (LPA-FLASH-RT protection pathway): The ultra-high dose rate maintains a low labile iron pool (Fe^{2+}) and suppresses ATF3 expression in the nucleus. This allows for continued transcription and function of the SLC7A11 transporter, promoting glutathione (GSH) synthesis. GSH inhibits reactive oxygen species (ROS) accumulation and lipid peroxidation, thereby preserving mitochondrial ultrastructure (intact cristae), maintaining high mitochondrial membrane potential (MMP) and ATP production, ultimately favoring cell survival. Right panel (CONV-RT ferroptosis pathway): Conventional irradiation leads to an expanded labile iron pool and upregulation of ATF3, which transcriptionally represses SLC7A11. The consequent failure of the antioxidant system drives iron-dependent Fenton reactions, leading to severe lipid peroxidation, mitochondrial dysfunction (loss of cristae, reduced MMP and ATP), and the execution of ferroptosis. Up arrows (↑) indicate upregulation or increase; down arrows (↓) indicate downregulation or decrease; crossed gene indicates transcriptional repression; crossed transporter indicates functional loss.

Furthermore, our results confirm that ferroptosis, rather than traditional apoptosis or necrosis, serves as the primary cell death pathway modulated by the FLASH effect in this nanosecond laser-proton regime. This claim offers an intriguing contrast to the recent work by Yan et al. [24], who demonstrated that

electron-driven FLASH-RT primarily regulates mitochondrial Cytochrome c leakage and subsequent caspase-mediated apoptosis. We proposed that this shift in execution pathways is fundamentally governed by the energy deposition density (ΔE). While electron beams are characterized by diffuse ionization and lower Linear Energy Transfer (LET)—with Geant4 Monte Carlo simulations showing ~1 keV in a 5 μm cell layer—our laser-accelerated protons deliver extreme instantaneous energy within localized volumes. According to our simulations, 7 MeV LPA-FLASH-RT protons traversing a 3.6 μm Mylar foil exhibit a peak energy deposition of 55 keV within a 5 μm cellular surrogate, corresponding to an effective LET of ~11 keV/μm. In comparison, 221 MeV clinical-energy protons yield a peak deposition of only ~13 keV (~2.6 keV/μm), indicating an approximately 4-fold increase in local energy deposition, which allows the effective LET of FLASH protons to approach to that of therapeutic heavy ions (for example, the LET in the plateau region of therapeutic carbon-ion beams is typically on the order of tens of keV/μm [25]). Moreover, both experimental measurements and simulations indicate that energy degradation in the solid-water phantom substantially reduces the number of protons reaching the cellular layer in the CONV-RT configuration, while simultaneously broadening the incident energy spectrum and the distribution of deposited energies. In contrast, FLASH-RT produces a relatively narrow incident energy spectrum, leading to more uniform energy deposition within the cellular layer (Figure 1c,e). The magnitude of ΔE serves as a physical switch for cell fate. The extreme ΔE of laser-protons induces immediate and catastrophic iron-dependent lipid peroxidation, while the lower ΔE of electrons triggers organized, protein-mediated signaling—the classic apoptotic cascade. This explains the difference against electron-driven FLASH-RT, and also suggests that the biological FLASH effect is not merely a function of the average high dose rate, but is intrinsically tied to the discrete spatial-temporal distribution of energy at the sub-cellular level.

Under conventional irradiation, radiation-induced DSBs activate metabolic reprogramming through the ATM–AMPK axis, which suppresses mTORC1-driven anabolic metabolism and redirects energy toward repair and the PARP1–NAD^+ axis, in which rapid NAD^+ consumption drives a compensatory glycolytic shift [26]. Given this established coupling between genotoxic stress and metabolic remodeling, a key question is whether the differential metabolic responses observed between A549 and BEAS-2B cells are driven by differences in DNA damage or reflect cell-intrinsic metabolic properties independent of genotoxic burden. The DNA damage data (Figure 2e,f) directly address this: no significant difference was detected between LPA-FLASH and CONV in either cell line, nor between the two cell types under equivalent irradiation. This equivalence of genotoxic load rules out differential DDR signaling as the proximal cause of the divergent metabolic phenotypes and implicates downstream metabolic buffering capacity as the primary determinant. The absence of dose-rate-dependent DNA damage differences is mechanistically consistent with the known limitations of in vitro systems: the FLASH-associated reduction in DNA damage observed *in vivo* is largely mediated by transient radiolytic oxygen depletion, a mechanism substantially attenuated in monolayer culture where dissolved oxygen is continuously replenished, and tissue-level oxygen gradients are absent [27]. Additionally, single time-point γ-H2AX quantification reflects residual unrepaired damage rather than initial break frequency. Tumor cells relying on Warburg-type glycolysis exhibit constrained mitochondrial flexibility and reduced antioxidant reserve, limiting their capacity to restore redox and bioenergetic homeostasis following radiation-induced oxidative perturbation; while normal epithelial cells retain greater mitochondrial reserve and engage SIRT1/AMPK-mediated metabolic recovery more effectively. This interpretation is further supported by a recent study demonstrating that FLASH selectively reduces lipid peroxidation in normal tissues while maintaining tumor cell ferroptosis, an effect determined by intrinsic differences in iron levels between cell types rather than by differential DNA damage [28]. Collectively, these findings suggest that cell-intrinsic metabolic and redox heterogeneity, rather than genotoxic burden, governs the differential response to LPA-FLASH-RT. To formally dissect the causal contribution of DNA damage signaling to these metabolic phenotypes, future studies should incorporate ATM or PARP inhibition combined with time-resolved metabolic profiling.

From a physico-chemical perspective, our data support a threshold-based rather than purely dose-proportional model for ROS signaling and lipid peroxidation under FLASH. In A549 cells, both LPA-FLASH-RT and CONV-RT drive ROS and downstream lipid peroxidation well above baseline, indicating that tumour cells, which exist in a state of pre-existing oxidative and iron stress, readily cross the execution threshold for ferroptosis under either dose-rate modality (Figure 3a–e). By contrast, in BEAS-2B cells, the nanosecond FLASH pulse elicits only a modest, transient ROS increase at 1 h, whereas CONV-RT generates a more sustained ROS elevation that is sufficient to trigger iron-dependent lipid peroxidation at 4 h (Figure 3a–e). This pattern is consistent with recent mechanistic work showing that ultra-high dose rate delivery reshapes radical–radical recombination and reduces the availability of long-lived diffusible ROS compared with conventional dose rates, and with *in vivo* evidence that FLASH limits lipid peroxidation in normal tissues while preserving ferroptotic killing in tumors in an iron-dependent manner [28,29]. Together with studies establishing that radiation-induced ferroptosis critically depends on ROS-driven lipid peroxidation and on lipid/antioxidant regulators such as ACSL4, SLC7A11 and GPX4, these findings support a model in which the discrete spatiotemporal pattern of ROS and lipid peroxidation under FLASH keeps normal cells below the kinetic and spatial thresholds required to ignite the ferroptotic cascade, while tumor cells still surpass these thresholds and undergo lethal ferroptosis [18,30].

The proton energy generated by our LPA system remains far below the 150–250 MeV level needed for deep-tumor proton therapy, which is why the present experiment was limited to single-layer cell irradiation with thin Mylar foils and a vacuum setup [13,31]. This limitation reflects the current energy ceiling of nanosecond laser-driven acceleration, especially in the Target Normal Sheath Acceleration (TNSA) regime, where proton energy scaling eventually saturates and further gain becomes inefficient [32,33]. At the same time, this should be viewed as a technical bottleneck rather than a fundamental barrier: recent advances in target engineering and laser control have already pushed laser-driven protons reaching 150 MeV and improved beam stability, showing that the field is moving toward higher-energy and more clinically relevant operation [14]. Therefore, while LPA-FLASH-RT is not yet ready for deep-tumor therapy, its compact geometry, controllability, and potential for further scaling make it a promising platform for future radiobiology studies and, eventually, clinical translation [34–36].

5. Conclusions

In summary, we demonstrate that laser-driven nanosecond FLASH-RT achieves a superior therapeutic window through a "temporal singularity"—the decoupling of ultra-fast radiolytic chemistry from biological stress sensing. By identifying ATF3 as a critical molecular time sensor, we reveal that FLASH protons exploit a transcriptional blind spot in normal cells, selectively aborting the iron-dependent ferroptotic cascade and mitochondrial collapse while maintaining active metabolic hormesis. This selectivity underscores that the FLASH effect is not merely a function of average dose rate, but is intrinsically governed by the sub-cellular spatial-temporal distribution of energy deposition (ΔE). These findings suggest that LPA-FLASH-RT may complement the traditional DNA-centric view of radiobiology by highlighting the role of metabolic regulation in cell fate determination, providing the scientific basis for next-generation, biomarker-guided radiotherapy.

Statement of the Use of Generative AI and AI-Assisted Technologies in the Writing Process

During the initial drafting phase of this manuscript, the authors used Claude Sonnet 5 (Anthropic) for language editing and proofreading to improve the clarity and readability of the text. The authors carefully reviewed and edited all suggestions provided by the tool, validated the accuracy of the content, and take full responsibility for the final manuscript.

Acknowledgments

The authors would like to thank the staff at the Super-Resolution Imaging Center of the University of Science and Technology of China (USTC) for their professional technical support and assistance with the imaging experiments.

Author Contributions

C.S., Y.Z. and P.H. contributed equally. Q.H., J.-H.B. and X.J. conceived and supervised the project. C.S. and X.Y. performed the investigations (biology). Y.Z., W.P., J.C., H.H. and J.-H.B. developed the methodology (laser physics & dosimetry). P.H., Y.W. and X.J. provided the resources (conventional irradiation). M.X., C.L., L.S., T.D. and X.M. handled data curation. C.S. and Y.Z. wrote the original draft. Q.H., J.-H.B. and X.J. reviewed and edited the manuscript.

Ethics Statement

Not applicable.

Informed Consent Statement

Not applicable.

Data Availability Statement

The data that support the findings of this study are available from the corresponding author upon reasonable request.

Funding

This work was supported by the National Key R&D Program of China (Grant No. 2025YFF0515103), the National Natural Science Foundation of China (Grant No. 42225405), the CAS Project for Young Scientists in Basic Research (Grant No. YSBR060), the Innovation Fund of the Anti-Radiation Application Technology Innovation Center of China Institute of Atomic Energy (Grant No. KFZC2023021002), and the Interdisciplinary Cultivation Program at Shandong University, Weihai.

Declaration of Competing Interest

The authors declare that they have no known competing financial interests or personal relationships that could have appeared to influence the work reported in this paper.

References

1. Citrin DE, Timmerman RD. Effects of radiotherapy in normal tissue. *N. Engl. J. Med.* **2026**, *394*, 996–1009. DOI:10.1056/NEJMra2506017
2. Favaudon V, Caplier L, Monceau V, Pouzoulet F, Sayarath M, Fouillade C, et al. Ultrahigh dose-rate FLASH irradiation increases the differential response between normal and tumor tissue in mice. *Sci. Transl. Med.* **2014**, *6*, 245ra93. DOI:10.1126/scitranslmed.3008973
3. Vozenin M-C, De Fornel P, Petersson K, Favaudon V, Jaccard M, Germond J-F, et al. The Advantage of FLASH Radiotherapy Confirmed in Mini-pig and Cat-cancer Patients. *Clin. Cancer Res.* **2019**, *25*, 35–42. DOI:10.1158/1078-0432.CCR-17-3375
4. Wilson JD, Hammond EM, Higgins GS, Petersson K. Ultra-high dose rate (FLASH) radiotherapy: Silver bullet or fool's gold? *Front. Oncol.* **2020**, *9*, 1563. DOI:10.3389/fonc.2019.01563
5. Montay-Gruel P, Petersson K, Jaccard M, Boivin G, Germond J-F, Petit B, et al. Irradiation in a flash: Unique sparing of memory in mice after whole brain irradiation with dose rates above 100 Gy/s. *Radiother. Oncol.* **2017**, *124*, 365–369. DOI:10.1016/j.radonc.2017.05.003

6. Montay-Gruel P, Acharya MM, Petersson K, Alikhani L, Yakkala C, Allen BD, et al. Long-term neurocognitive benefits of FLASH radiotherapy driven by reduced reactive oxygen species. *Proc. Natl. Acad. Sci. USA* **2019**, *116*, 10943–10951. DOI:10.1073/pnas.1901777116
7. Bourhis J, Sozzi WJ, Jorge PG, Gaide O, Bailat C, Duclos F, et al. Treatment of a first patient with FLASH-radiotherapy. *Radiother. Oncol. J. Eur. Soc. Ther. Radiol. Oncol.* **2019**, *139*, 18–22. DOI:10.1016/j.radonc.2019.06.019
8. Spitz DR, Buettner GR, Petronek MS, St-Aubin JJ, Flynn RT, Waldron TJ, et al. An integrated physico-chemical approach for explaining the differential impact of FLASH versus conventional dose rate irradiation on cancer and normal tissue responses. *Radiother. Oncol.* **2019**, *139*, 23–27. DOI:10.1016/j.radonc.2019.03.028
9. Cao X, Zhang R, Esipova TV, Allu SR, Ashraf R, Rahman M, et al. Quantification of oxygen depletion during FLASH irradiation *in vitro* and *in vivo*. *Int. J. Radiat. Oncol. Biol. Phys.* **2021**, *111*, 240–248. DOI:10.1016/j.ijrobp.2021.03.056
10. Allen BD, Acharya MM, Montay-Gruel P, Jorge PG, Bailat C, Petit B, et al. Maintenance of tight junction integrity in the absence of vascular dilation in the brain of mice exposed to ultra-high-dose-rate FLASH irradiation. *Radiat. Res.* **2020**, *194*, 625–635. DOI:10.1667/RADE-20-00060.1
11. Dixon SJ, Lemberg KM, Lamprecht MR, Skouta R, Zaitsev EM, Gleason CE, et al. Ferroptosis: An iron-dependent form of non-apoptotic cell death. *Cell* **2012**, *149*, 1060–1072. DOI:10.1016/j.cell.2012.03.042
12. Montay-Gruel P, Markarian M, Allen BD, Baddour JD, Giedzinski E, Goncalves Jorge P, et al. Ultra-high-dose-rate FLASH irradiation limits reactive gliosis in the brain. *Radiat. Res.* **2020**, *194*, 636–645. DOI:10.1667/RADE-20-00067.1
13. Bin J, Obst-Huebl L, Mao J-H, Nakamura K, Geulig LD, Chang H, et al. A new platform for ultra-high dose rate radiobiological research using the BELLA PW laser proton beamline. *Sci. Rep.* **2022**, *12*, 1484. DOI:10.1038/s41598-022-05181-3
14. Ziegler T, Göthel I, Assenbaum S, Bernert C, Brack F-E, Cowan TE, et al. Laser-driven high-energy proton beams from cascaded acceleration regimes. *Nat. Phys.* **2024**, *20*, 1211–1216. DOI:10.1038/s41567-024-02505-0
15. Snavely RA, Key MH, Hatchett SP, Cowan TE, Roth M, Phillips TW, et al. Intense high-energy proton beams from petawatt-laser irradiation of solids. *Phys. Rev. Lett.* **2000**, *85*, 2945–2948. DOI:10.1103/PhysRevLett.85.2945
16. Xu Y, Lu J, Li W, Wu F, Li Y, et al. A stable 200TW/1 Hz Ti:sapphire laser for driving full coherent XFEL. *Opt. Laser Technol.* **2016**, *79*, 141–145. DOI: 10.1016/j.optlastec.2015.11.023
17. Wu F, Zhang Z, Yang X, Hu J, Ji P, et al. Performance improvement of a 200TW/1Hz Ti:sapphire laser for laser wakefield electron accelerator. *Opt. Laser Technol*. **2020**, *131*, 106453. DOI:10.1016/j.optlastec.2020.106453
18. Vozenin M-C, Montay-Gruel P, Tsoutsou P, Limoli CL. Mechanisms, challenges and opportunities for FLASH radiotherapy in cancer. *Nat. Rev. Cancer* **2026**, *26*, 62–75. DOI:10.1038/s41568-025-00878-9
19. Kacem H, Kunz L, Korysko P, Ollivier J, Tsoutsou P, Martinotti A, et al. Modification of the microstructure of the CERN-CLEAR-VHEE beam at the picosecond scale modifies ZFE morphogenesis but has no impact on hydrogen peroxide production. *Radiother. Oncol.* **2025**, *209*, 110942. DOI:10.1016/j.radonc.2025.110942
20. Lei G, Zhang Y, Koppula P, Liu X, Zhang J, Lin SH, et al. The role of ferroptosis in ionizing radiation-induced cell death and tumor suppression. *Cell Res.* **2020**, *30*, 146–162. DOI:10.1038/s41422-019-0263-3
21. Doll S, Proneth B, Tyurina YY, Panzilius E, Kobayashi S, Ingold I, et al. ACSL4 dictates ferroptosis sensitivity by shaping cellular lipid composition. *Nat. Chem. Biol.* **2017**, *13*, 91–98. DOI:10.1038/nchembio.2239
22. Lang X, Green MD, Wang W, Yu J, Choi JE, Jiang L, et al. Radiotherapy and immunotherapy promote tumoral lipid oxidation and ferroptosis via synergistic repression of SLC7A11. *Cancer Discov.* **2019**, *9*, 1673–1685. DOI:10.1158/2159-8290.CD-19-0338
23. Kim J, DeBerardinis RJ. Mechanisms and implications of metabolic heterogeneity in cancer. *Cell Metab.* **2019**, *30*, 434–446. DOI:10.1016/j.cmet.2019.08.013
24. Lv J, Sun J, Luo Y, Liu J, Wu D, Fang Y, et al. Ultrahigh dose rate irradiation regulates mitochondrial DNA-induced interferon-β secretion via cytochrome c leakage. *Med. Comm.* **2025**, *6*, e70457. DOI:10.1002/mco2.70457
25. Durante M, Debus J, Loeffler JS. Physics and biomedical challenges of cancer therapy with accelerated heavy ions. *Nat. Rev. Phys.* **2021**, *3*, 777–790. DOI:10.1038/s42254-021-00368-5
26. Murata MM, Kong X, Moncada E, Chen Y, Imamura H, Wang P, et al. NAD+ consumption by PARP1 in response to DNA damage triggers metabolic shift critical for damaged cell survival. *Mol. Biol. Cell* **2019**, *30*, 2584–2597. DOI:10.1091/mbc.E18-10-0650
27. Cooper CR, Jones D, Jones GD, Petersson K. FLASH irradiation induces lower levels of DNA damage *ex vivo*, an effect modulated by oxygen tension, dose, and dose rate. *Br. J. Radiol.* **2022**, *95*, 20211150. DOI:10.1259/bjr.20211150
28. Vilaplana-Lopera N, Kim J, Nam G, Tullis IDC, Paillas S, Ruan J-L, et al. Tissue-specific iron levels modulate lipid peroxidation and the FLASH radiotherapy effect. *Cell Death Dis.* **2025**, *16*, 668. DOI:10.1038/s41419-025-07988-0
29. Yang Y, Yin F-F. Understanding of FLASH radiotherapy through physical to biological interpretation. *Radiat. Med. Prot.* **2025**, *6*, 187–195. DOI:10.1016/j.radmp.2025.07.002
30. Wang F, Dai Q, Xu L, Gan L, Shi Y, Yang M, et al. Advances on the role of ferroptosis in ionizing radiation response. *Curr.*

Pharm. Biotechnol. **2024**, *25*, 396–410. DOI:10.2174/1389201024666230823091144
31. Bin J, Klaus A, Assmann W, Dollinger G, Guido AD, et al. A laser-driven nanosecond proton source for radiobiological studies. *Appl. Phys. Lett.* **2012**, *101*, 243701. DOI:10.1063/1.4769372
32. McKenna P, Robson L, Diesen J, Foster JM, et al. Review of laser-driven ion sources and their applications. *Rep. Prog. Phys.* **2012**, *75*, 056401. DOI:10.1088/0034-4885/75/5/056401
33. Macchi A, Borghesi M, Passoni M. Ion acceleration by superintense laser-plasma interaction. *Rev. Mod. Phys*. **2013**, *85*, 751–793. DOI:10.1103/RevModPhys.85.751
34. Linz U, Alonso J. What will it take for laser driven proton accelerators to be applied to tumor therapy? *Phys. Rev. ST Accel. Beams* **2007**, *10*, 094801. DOI:10.1103/PhysRevSTAB.10.094801
35. Schreiber J, Bolton P, Parodi K. Invited review article: "Hands-on" laser-driven ion acceleration: A primer for laser-driven source development and potential applications. *Rev. Sci. Instrum.* **2016**, *87*, 071101. DOI:10.1063/1.4959198
36. Tajima T, Habs D, Yan X. Laser acceleration of ions for radiation therapy. *Rev. Accel. Sci. Tech.* **2009**, *2*, 201. DOI:10.1142/S1793626809000296